

# PGIR 20eid (SN 2020qmp): A Type II-P Supernova at 15.6 Mpc discovered by the Palomar Gattini-IR survey

G. P. Srinivasaragavan<sup>1</sup>, I. Sfaradi<sup>2</sup>, J. Jencson<sup>3</sup>, K. De<sup>1</sup>, A. Horesh<sup>2</sup>, M. M. Kasliwal<sup>1</sup>, S. Tinyanont<sup>4</sup>, M. Hankins<sup>5</sup>, S. Schulze<sup>6</sup>, M. C. B. Ashley<sup>7</sup>, M. J. Graham<sup>2</sup>, V. Karambelkar<sup>1</sup>, R. Lau<sup>8</sup>, A. A. Mahabal<sup>9,10</sup>, A. M. Moore<sup>11</sup>, E. O. Ofek<sup>12</sup>, Y. Sharma<sup>1</sup>, J. Sollerman<sup>13</sup>, J. Soon<sup>11</sup>, T. Travouillon<sup>11</sup>, and R. Walters<sup>14</sup>

<sup>1</sup> Cahill Center for Astrophysics, California Institute of Technology, 1200 E. California Blvd, Pasadena, CA 91125, USA

<sup>2</sup> Racah Institute of Physics, The Hebrew University of Jerusalem, Jerusalem 91904, Israel

<sup>3</sup> Steward Observatory, University of Arizona, 933 North Cherry Avenue, Rm. N204, Tucson, AZ 85721-0065, USA

<sup>4</sup> Department of Astronomy and Astrophysics, University of California, Santa Cruz, CA 95064, USA

<sup>5</sup> The Department of Physical Sciences, Arkansas Tech University, 215 West O Street, Russellville, AR 72801, USA

<sup>6</sup> The Oskar Klein Centre, Physics Department, Stockholm University, AlbaNova University Centre, SE 106 91 Stockholm, Sweden

<sup>7</sup> School of Physics, University of New South Wales, Sydney NSW 2052, Australia

<sup>8</sup> Institute of Space & Astronautical Science, Japan Aerospace Exploration Agency, 3-1-1 Yoshinodai, Chuo-ku, Sagamihara, Kanagawa 252-5210, Japan

<sup>9</sup> Division of Physics, Mathematics and Astronomy, California Institute of Technology, Pasadena, CA 91125, USA

<sup>10</sup> Center for Data Driven Discovery, California Institute of Technology, Pasadena, CA 91125, USA

<sup>11</sup> Research School of Astronomy and Astrophysics, Australian National University, Canberra, ACT 2611, Australia

<sup>12</sup> Benoziyo Center for Astrophysics, Weizmann Institute of Science, 76100 Rehovot, Israel

<sup>13</sup> The Oskar Klein Centre, Department of Astronomy, Stockholm University, AlbaNova, SE-106 91 Stockholm, Sweden

<sup>14</sup> Caltech Optical Observatories, California Institute of Technology, Pasadena, CA 91125, USA

## ABSTRACT

**Aims.** We present a detailed analysis of SN 2020qmp, a nearby Type II-P core-collapse supernova (CCSN), discovered by the Palomar Gattini-IR (PGIR) survey in the galaxy UGC07125 (distance of  $\approx 15.6 \pm 4$  Mpc). We illustrate how the multiwavelength study of this event helps our general understanding of stellar progenitors and circumstellar medium (CSM) interactions in CCSNe. We highlight the importance of near-infrared (NIR) surveys for early detections of SNe in dusty environments.

**Methods.** We analyze data from observations in various bands: radio, NIR, optical and X-rays. We use optical and NIR data for a spectroscopic and spectro-polarimetric study of the SN, and to model its lightcurve (LC). We estimate the explosion energy and zero-age main sequence (ZAMS) progenitor mass through hydrodynamical LC modeling. We also obtain an independent estimate of the ZAMS progenitor mass from the luminosity of the [O I] doublet lines ( $\lambda\lambda 6300, 6364$ ) normalized to the decay power of  $^{56}\text{Co}$ . From radio and X-ray observations, we derive the mass loss rate and microphysical parameters of the progenitor star, and investigate possible deviations from energy equipartition of magnetic fields and electrons in a standard CSM interaction model. Finally, we simulate a sample of CCSNe with plausible distributions of brightness and extinction, within 40 Mpc, and test what fraction of the sample is detectable at peak light by NIR surveys versus optical surveys.

**Results.** SN 2020qmp displays characteristic hydrogen lines in its optical spectra, as well as a plateau in its optical LC, hallmarks of a Type II-P SN. We do not detect linear polarization during the plateau phase, with a  $3\sigma$  upper limit of 0.78%. Through hydrodynamical LC modeling and an analysis of its nebular spectra, we estimate a progenitor mass of around  $12 M_{\odot}$ , and an explosion energy of around  $0.5 \times 10^{51}$  erg. We find that the spectral energy distribution cannot be explained by a simple CSM interaction model, assuming a constant shock velocity and steady mass-loss rate. In particular, the excess X-ray luminosity compared with the synchrotron radio luminosity suggests deviations from equipartition. Finally, we demonstrate the advantages of NIR surveys over optical surveys for the detection of dust-obscured CCSNe in the local universe. Specifically, our simulations show that the Wide-Field Infrared Transient Explorer (WINTER) will detect about 14 more CCSNe out of 75 expected in its footprint within 40 Mpc, over five years than an optical survey equivalent to the Zwicky Transient Facility (ZTF) would detect.

**Conclusions.** We have determined or constrained the main properties of SN 2020qmp and of its progenitor, highlighting the value of multiwavelength follow up observations of nearby CCSNe. We have shown that forthcoming NIR surveys will finally enable us to do a nearly complete census of CCSNe in the local universe.

**Key words.** stars: supernovae - stars: circumstellar matter- shock waves

## 1. Introduction

Type II supernovae (SNe) are hydrogen-rich core-collapse supernovae (CCSNe) that represent the fate of stars that have a minimum mass of around 7 to  $9 M_{\odot}$  (Smartt 2009), though the maximum mass of CCSN progenitors is a debated topic (Utrobin & Chugai 2009; Dessart et al. 2010; Jerkstrand et al. 2012). The

Type II class is divided observationally into many different subclasses based on their lightcurves (LCs) and spectroscopic properties, including Type IIP, IIL, and IIn, and IIb (Gal-Yam 2017). Of these, Type IIP events characterized by a plateau in their optical LCs lasting about 100 days after the explosion, are most common (Branch & Wheeler 2017).

Though Type IIP SNe are among the most common SNe found, it is uncommon to discover nearby CCSNe (only five during the past three years within 10 Mpc reported to the Transient Name Server<sup>1</sup>). Nearby and bright CCSNe allow us to probe many different facets of SN physics, including obtaining high-resolution spectra for astrochemistry purposes (Shivvers et al. 2015), astrometric pinpointing of the progenitor star (Smartt 2009, 2015), analyzing the physics of the shock breakout (Rabinak & Waxman 2011; Sapir & Waxman 2017), understanding the polarimetry of the SN (eg. Leonard et al. 2006; Wang & Wheeler 2008; Nagao et al. 2017, 2018; Tinyanont et al. 2019) and opening the avenue for multi-messenger follow up on the sources (Nakamura et al. 2016). Furthermore, the interaction between the blast wave of CCSNe and the circumstellar or interstellar medium (CSM or ISM) generates multi-wavelength emission through synchrotron radiation processes (Chevalier 1998). Observing this synchrotron radiation, mainly in the radio and X-ray, provides key insights into the progenitor star's final years, and allows us to probe the very late stages of stellar evolution of massive stars (Berger et al. 2002; Ben-Ami et al. 2012; Horesh et al. 2013a).

Palomar Gattini-IR (PGIR; Moore & Kasliwal 2019; De et al. 2020a) is a wide-field near-infrared (NIR) time-domain survey that is able to image three-fourths of the entire night sky on a given night. Located at Palomar observatory, PGIR uses a telescope with an aperture of 300 mm, and a camera field of view of 25 square degrees, along with a HAWAII-2RG detector that operates in a single  $J$  band filter (De et al. 2020a). PGIR has a median cadence of 2 days, and can image sources up to a median depth of 15.7 AB mag (De et al. 2020a) in  $J$  band. As a wide and shallow IR time domain survey, PGIR is sensitive to NIR bright transients in the Milky Way and nearby galaxies, including events that could be missed in the optical due to a large extinction.

On UT 2020-07-30 (all dates in the rest of the paper are in UT time), PGIR made its first extragalactic discovery of a SN with its detection of PGIR 20eid (SN 2020qmp), which was spectroscopically classified as a Type II-P SN (De et al. 2020b). In this paper, we present the NIR and optical LCs and spectroscopy of the SN up to the first 244 days of its evolution. We then analyze the optical spectra of the SN after it has reached its nebular phase, in order to infer the mass of the progenitor star. We also present radio data obtained from the Karl G. Jansky Very Large Array (VLA), and *Swift* X-ray data, which allowed us to infer key characteristics pertaining to properties of the SN blast wave and its interaction with materials lost from the progenitor star during the late stages of its life. Finally we comment on the local CCSN rate, and how NIR surveys are well equipped to find optically obscured CCSNe in the future due to their ability to see through large amounts of dust extinction.

The paper is organized as follows. In §2, we present the observations in the ultraviolet (UV), optical, and NIR by the Neil Gehrels *Swift* Observatory (*Swift*; Gehrels et al. 2004) the Zwicky Transient Facility (ZTF; Bellm et al. 2019; Graham et al. 2019; Masci et al. 2019; Dekany et al. 2020), and PGIR, along with its optical and NIR spectra and radio observations. In §3, we present comparisons of hydrodynamical LC models to the observed LCs of the SN in order to infer the zero-age main sequence (ZAMS) progenitor mass along with the explosion energy of the SN. In §4, we analyze the nebular spectra of the SN and compare it with model spectra, in order to also infer the ZAMS progenitor mass using an independent method. In §5,

we present the analysis from the radio and X-ray data, and infer various properties of the blast wave and progenitor star's mass loss rate, as well as possible deviations from a standard CSM interaction model. In §6 we describe the local CCSN rate and examine the sensitivity of PGIR to highly extinguished SNe in the local universe compared to optical searches. Finally, in §7, we summarize the main conclusions of our results.

## 2. Observations of SN 2020qmp

### 2.1. Photometric and X-Ray Observations

SN 2020qmp was first discovered in the automated image subtraction and transient detection pipeline of the PGIR survey on 2020-07-30, at a (RA, Dec) of  $(12^{\text{h}}08^{\text{m}}44.43^{\text{s}}, +36:48:19.4)$  at magnitude  $J = 14.74 \pm 0.2$  AB mag (all magnitudes for the rest of the paper are in units of AB mag, unless specified otherwise). This source was detected as part of a search for large amplitude transients described in (De et al. 2021). The transient was detected on the spiral arm of galaxy UGC07125, which has a distance of 15.6 Mpc, and a distance modulus of  $m - M = 30.97 \pm 0.54$  mag (Tully et al. 2016), which is a fairly large distance uncertainty. Assuming this distance, the absolute magnitude of the transient upon first detection was  $M = -15.7$  in  $J$  band. The latest non-detection by PGIR was on 2020-07-25, up to a  $5\sigma$  limiting magnitude of  $J = 15.1$  mag, which is five days before the first detection due to the low visibility of the field, as it was close to the Sun. The discovery location of the SN by PGIR, along with an image from the Pan-STARRS1 survey (Kaiser et al. 2002) are shown for reference in Figure 1.

Though PGIR made the initial discovery of the SN, a search in ZTF data at the same position revealed an even earlier detection of the SN on 2020-07-26 (ZTF20abotkfn; De et al. 2020b). The latest non-detection by ZTF was on 2020-07-22, up to a limiting magnitude of  $i = 19.1$  mag. We estimate the explosion date to be the average of the latest non-detection by ZTF and the first detection, on 2020-07-24 ( $\pm 2$  days). All mentions of "days" used in figures are with reference to this explosion date. ZTF continued to observe the SN in the  $g$ ,  $r$ , and  $i$ -bands.

Following the initial announcement of the discovery (De et al. 2020b), the transient was followed up by *Swift* using the Ultra-Violet Optical telescope (UVOT; Roming et al. 2005) and the X-ray telescope (XRT; Burrows et al. 2005). *Swift* observed the field with UVOT between 31 July and 8 August 2020 (PI: Paraskeva). The brightness in the UVOT filters was measured with UVOT-specific tools in the package HEASOFT<sup>2</sup> version 6.26.1. Source counts were extracted from the images using a  $3''$  radius aperture. The background was estimated using a circular region with a radius of  $29''$  close to the SN position. The count rates were obtained from the images using the *Swift* tool `uvotsource`. They were converted to magnitudes using the UVOT photometric zero points (Breeveld et al. 2011). Due to the lack of host templates, the SN flux includes the contribution from the host galaxy. All magnitudes were transformed into the AB system using Breeveld et al. (2011).

*Swift*/XRT observed the SN in the energy range from 0.3 to 10 keV. We analyzed all data with the online-tools of the UK *Swift* team<sup>3</sup> that use the methods described in Evans et al. (2007) and Evans et al. (2009) and HEASOFT. Combining the four epochs taken in July/August 2020 amounts to a total XRT exposure time of 3982 s, and provides a marginal detection of

<sup>2</sup> <https://heasarc.gsfc.nasa.gov/docs/software/heasoft/>

<sup>3</sup> [https://www.swift.ac.uk/user\\_objects/](https://www.swift.ac.uk/user_objects/)

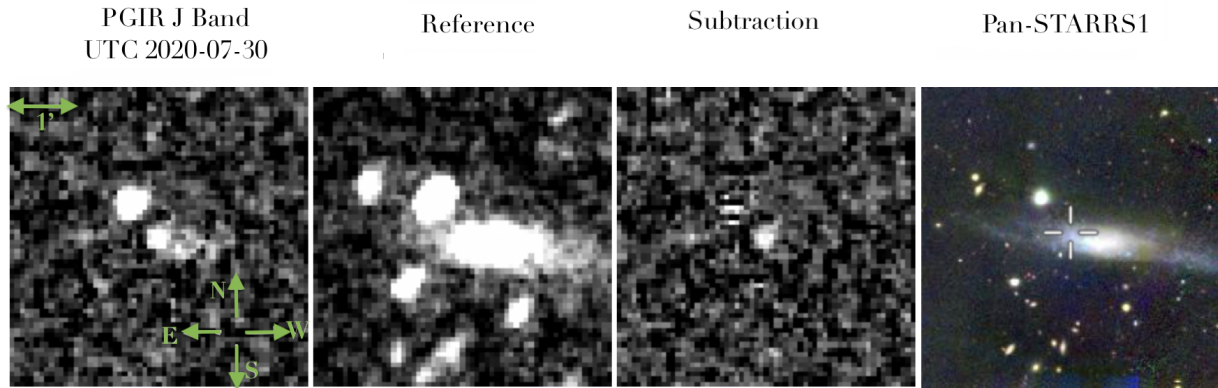


**Fig. 1.** Discovery location of SN 2020qmp, containing images from the night of discovery (2020-07-30) taken by PGIR. The left frame is the first detection, the next frame to the right is a reference template image constructed from stacking previous PGIR images, the subtraction image clearly shows the source coincident with the host galaxy. A pre-explosion optical image from Pan-STARRS1 is shown for comparison, with a cross-hairs in the position of the SN.

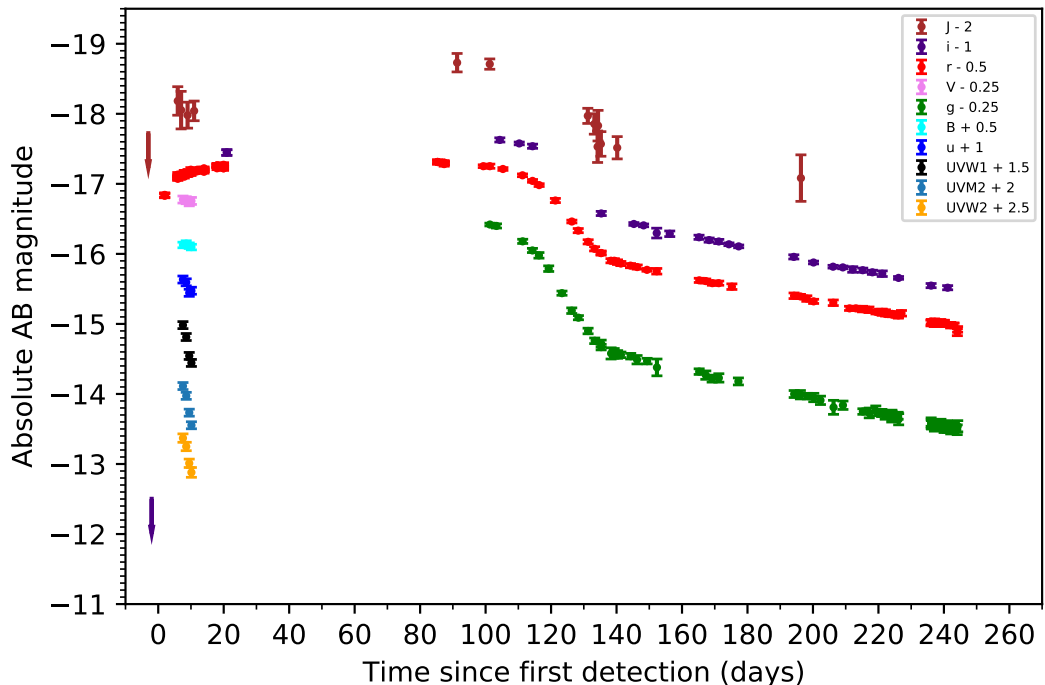


**Fig. 2.** Light curve of SN 2020qmp. The light curve includes photometry points from the PGIR survey (*J*-band) as well as the *Swift* UVOT telescope (*UVW1*, *UVM2*, *UVW2*, *u*, *B*, and *V* bands), and ZTF (*g*, *r* and *i* bands).

$0.0014^{+0.0009}_{-0.0007}$  count  $\text{s}^{-1}$  between 0.3 and 10 keV. If we assume a power-law spectrum with a photon index of  $\Gamma = 2$  and a Galactic hydrogen column density of  $1.95 \times 10^{20} \text{ cm}^{-2}$  (HI4PI Collaboration et al. 2016) this corresponds to an unabsorbed 0.3–10.0 keV flux of  $5.1^{+3.3}_{-2.6} \times 10^{-14} \text{ erg cm}^{-2} \text{ s}^{-1}$ . At the luminosity distance of SN 2020qmp this corresponds to a luminosity of  $L_X = 2 \pm 1 \times 10^{39} \text{ erg s}^{-1}$  (0.3–10 keV) on 2020-08-02. A final 4.8-ks observation was obtained on 2020-12-19. The source was not detected in X-rays. The 3- $\sigma$  count-rate limit is  $0.002 \text{ ct s}^{-1}$ . Using the same model as for the early-time observations, the luminosity is  $< 2.3 \times 10^{39} \text{ erg s}^{-1}$  between 0.3 and 10 keV.

The LC of the SN over a range of wavelengths is shown in Figure 2. We also calculated the bolometric LC of the SN by performing a black body fit with all available filters at every photometric epoch available, and then integrating the black body to derive a luminosity. In the early-time LC during the first 20 days after explosion, we use photometry within one day windows to calculate our black body fits, as the early-time LC is very variable. After 20 days, we use photometry within four day windows, and then perform black body fits for every day there are at least three different wavelength bands available. The bolometric LC is presented in Figure 3.

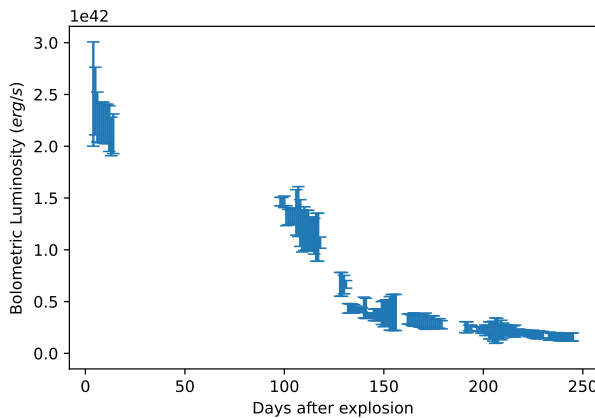


**Fig. 3.** The bolometric LC of SN 2020qmp.

## 2.2. Spectroscopy and Classification

We initiated rapid spectroscopic follow-up of the transient after the initial detection with the SED Machine spectograph (SEDM); (Blagorodnova et al. 2018; Rigault et al. 2019) on the Palomar 60 inch telescope (on 2020-07-31), the Gemini Multi-object Spectrograph on the North Gemini telescope (Sivanandam et al. 2018) (on 2020-07-31) and the Double Beam Spectrograph (DBSP, Oke & Gunn 1982) on the Palomar 200-inch telescope (on 2020-08-12). We show the spectral evolution in Figure 4. The presence of Balmer lines ( $H\alpha$  and  $H\beta$  labeled in Figure 4) points towards the classification of a Type II SN (Filippenko 1997; Gal-Yam 2017). Our spectra also show evidence for P-Cygni profiles from He I and Ca II. The relatively flat light curve is characteristic of the plateau of constant brightness found in Type IIP SNe, typically expected to last around 100 days (Branch & Wheeler 2017). Taken together, we classify SN 2020qmp as a Type IIP SN. Using the minimum of the strong P-Cygni profile of the  $H\alpha$  line, we see that the photospheric velocities decrease over time. We measured a photospheric velocity of  $9400 \text{ km s}^{-1}$  in the first SEDM spectrum,  $8800 \text{ km s}^{-1}$  in the Gemini spectrum, and  $7900 \text{ km s}^{-1}$  in the first P200 spectrum.

We also obtain four additional optical spectra, from SEDM again (on 2020-08-28), from the Low Resolution Imaging Spectograph on the Keck-I telescope (LRIS; Oke et al. 1995 on 2020-11-20), and three more from DBSP (on 2021-01-08, 2021-02-20, and 2021-04-16). The latter four spectra show the transition of the SN into the radioactive decay nebular phase, with characteristic nebular spectra features like the [O I] doublet ( $\lambda\lambda 6300, 6364 \text{ \AA}$ ) which strengthens with time as the SN progresses into the nebular phase (see § 4).

Four spectra in the NIR were also obtained. These were obtained with the Near-Infrared Echelle Spectrometer (NIRES; Martin et al. 2018), on 2020-10-31, the Triple Spectrograph on the Palomar 200 inch Telescope (TSPEC; Herter et al. 2008), on 2020-12-22 and 2021-02-04, and the NASA Infrared Telescope Facility SpeX instrument (IRTF + SpeX; Rayner et al. 2003), on 2021-05-16) as part of program 2020A111 (PI: K. De). All spectra obtained are shown in Figure 4.

## 2.3. Near-Infrared Spectropolarimetry

The proximity and brightness of SN 2020qmp allowed for spectropolarimetry observations in the IR. Spectropolarimetric observations can constrain the geometry of the ionized, electron

scattering region in the SN. NIR spectropolarimetry has an added benefit of less contamination from dust polarization along the line of sight, both in the host galaxy and in the Milky Way (Nagao et al. 2018). We observed the SN on 2020-10-29, 91 days post-discovery, while the SN was still in the plateau phase, with the apparent magnitude of  $J = 13.2$  mags. The observation was obtained using the IR spectropolarimeter WIRC+Pol on the 200-inch telescope at Palomar Observatory (Tinayanont et al. 2019). The SN was observed inside its  $3''$  wide slit in an ABAB dithering pattern for the total of 64 min of exposure time. The observations were performed at high airmass (average of 1.8), resulting in low flux due to the large atmospheric extinction. WIRC+Pol exhibits  $<0.03\%$  of instrumental polarization, and observations of unpolarized standard stars were not necessary (Tinayanont et al. 2019). The data were reduced using the WIRC+Pol data reduction pipeline.<sup>4</sup>

Figure 5 shows the normalized Stokes parameters (values describing the state of polarization present in the electromagnetic radiation being studied)  $q$  and  $u$  plotted against each other, color-coded by wavelength. On this plot, the distance from origin is the degree of polarization  $p$  while the angle with respect to the  $x$  axis is twice the angle of polarization  $\theta$ . We did not detect polarization from SN 2020qmp, as the broadband degree of polarization was  $0.14 \pm 0.26\%$ , making the SN unpolarized to within 0.78% at the  $3\sigma$  level. The typical error bar per spectral channel is 1% in both  $q$  and  $u$ , and the broadband upper limits are 0.25% and 0.27% in  $q$  and  $u$ , respectively (all  $1\sigma$ ). The non-detection of polarization of a SN II-P during the plateau phase is consistent with most Type II-P SNe because the outer ejecta, visible during this phase, are generally symmetric (see review by Wang & Wheeler 2008).

## 2.4. Observations by the VLA

The VLA observed (under our DDT program VLA/20B-398; PI Horesh) the field of SN 2020qmp and detected radio emission consistent with the SN position in four epochs. The first observation, on 2020-09-13, showed a point source in both C band (6 GHz) and K band (22 GHz), at a flux level of 0.25 and 0.08 mJy respectively. The detection image in C band is shown in Figure 6. We continued monitoring the SN with the VLA using S, C, X, and Ku bands (3, 6, 10, and 15 GHz), for three additional epochs up to 136 days post explosion.

We calibrated our observations with the automated VLA calibration pipeline available in the Common Astronomy Software Applications (CASA) package (McMullin et al. 2007). 3C286 was used as the primary flux calibrator, while J1146+3958 was used as the gain calibrator. When imaging the field of SN 2020qmp with the CASA task CLEAN, we divided C and S bands into two sub-bands when the signal-to-noise ratio was high enough. We used the CASA task IMFIT to fit the source in the phase center and to extract the peak flux density. We estimate its error as the square root of the quadratic sum of the error produced by the CASA task IMFIT, the image rms produced by the CASA task IMSTAT, and 10% calibration error. We report the flux density measurement in §5 and in Table 1.

## 3. Hydrodynamical LC Modeling

It is possible to constrain the ZAMS progenitor mass and initial explosion energy of the SN through hydrodynamical LC modeling (Utrobin & Chugai 2015, 2017; Morozova et al. 2017, 2018;

<sup>4</sup> [https://github.com/WIRC-Pol/wirc\\_drp](https://github.com/WIRC-Pol/wirc_drp)

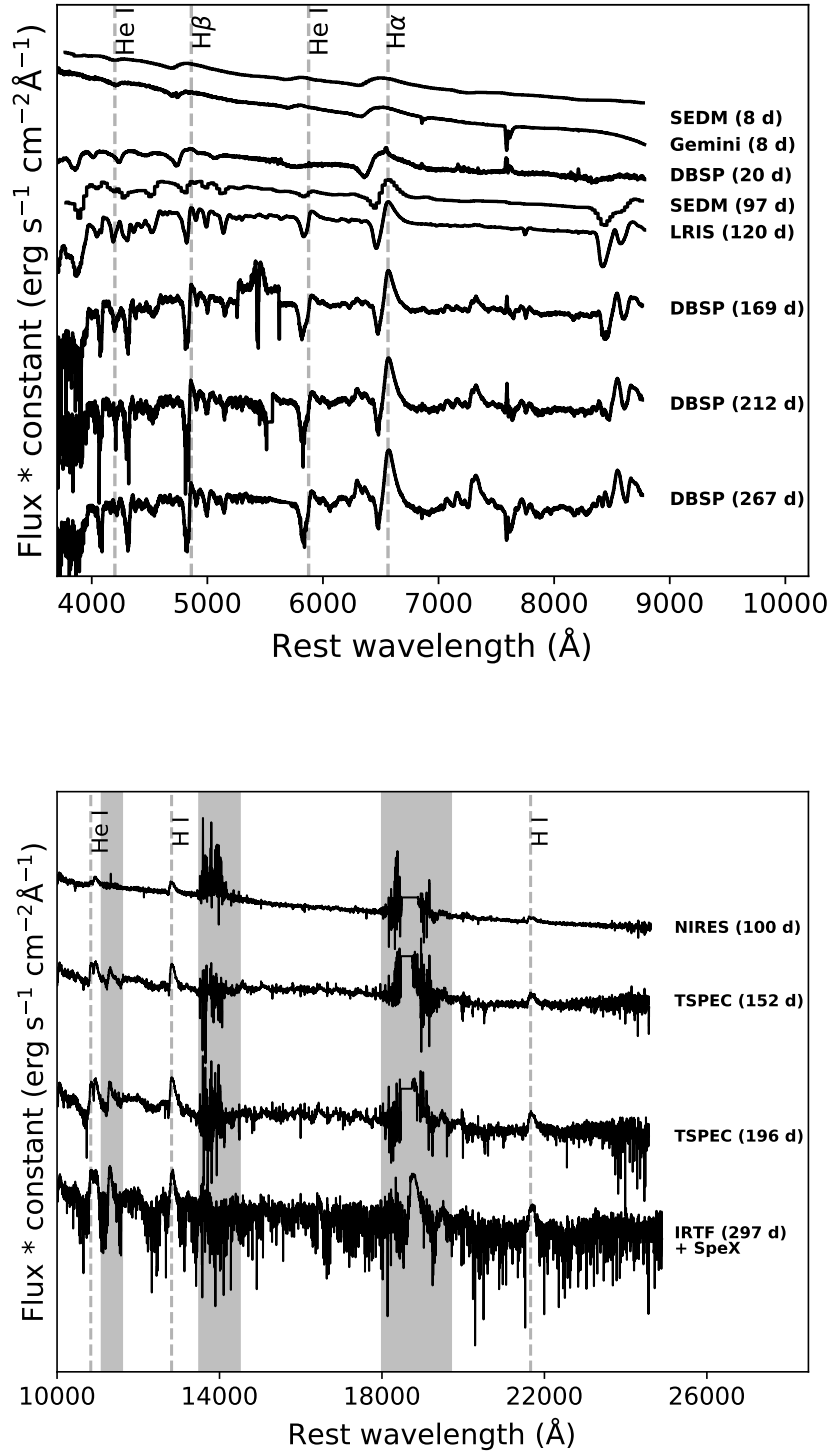


**Fig. 4.** *Top panel:* Spectral evolution in the optical of SN 2020qmp. The most prominent spectral features are labeled, with the instruments and phases shown to the right of the spectrum. *Bottom panel:* Spectral evolution in the NIR of SN 2020qmp, with the same labels in the top panel. Areas of atmospheric absorption are grayed out.

Goldberg et al. 2019; Martinez & Bersten 2019). In order to do so, we use the open-source SN Explosion Code (SNEC; Morozova et al. 2015). SNEC assumes local thermodynamic equilibrium (LTE) and diffusive radiative transport, and these assumptions allow it to model LCs well up to the radioactive de-

cay phase, where these assumptions break down. Therefore, we only compare the model LCs generated through SNEC to the observed LCs up to 125 days after the explosion, when the plateau phase has noticeably transitioned to the optically thin nebular phase.

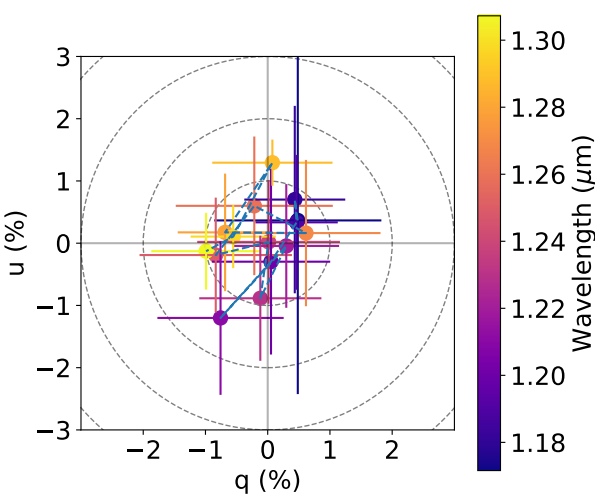


**Fig. 5.** J-Band spectropolarimetry of SN 2020qmp conducted using WIRC+POL, on 2020-08-29. The panel shows the q-u plane, color coded by wavelength, and isolines of constant polarization.

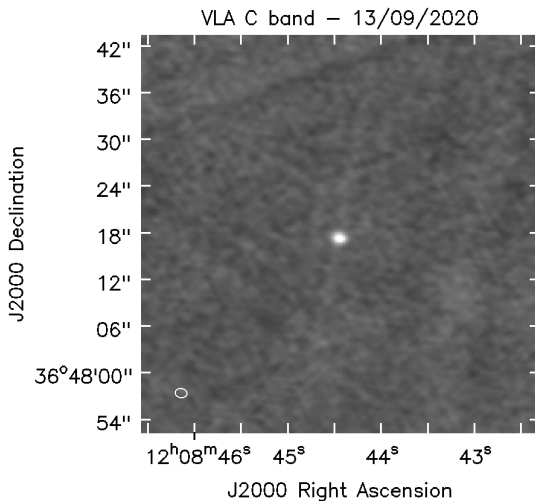


**Fig. 6.** Image of SN 2020qmp in C band by the VLA on 2020-09-13.

In our analysis, we follow a similar approach to Morozova et al. (2017), and began by generating optical LCs corresponding to a range of ZAMS progenitor masses between  $10.0 M_{\odot}$  and  $17.5 M_{\odot}$  ( $\Delta M = 2.5 M_{\odot}$ ), and a range of explosion energies between  $0.2$  and  $1.2 \times 10^{51}$  erg ( $\Delta E = 0.4 \times 10^{51}$  erg) with stellar structure models obtained from Sukhbold et al. (2016). We fix the  $^{56}\text{Ni}$  mass of the models to  $M_{\text{Ni}} = 0.06 M_{\odot}$ , which we obtained using photometry on the radioactive decay tail (see §4). We then run through a coarse grid of models and perform a  $\chi^2$  analysis between the models and the observed LCs in the  $g$ ,  $r$ , and  $i$ -bands. This  $\chi^2$  analysis is done through comparing every observed photometry point from the ZTF LC to the model point equivalent in time to the observed point, corresponding to the same band filter. The models generate photometry points in units of absolute AB magnitudes, so we convert the model points to apparent AB magnitudes to display in Figure 7, but perform the  $\chi^2$  analysis in flux space after converting the apparent AB magnitudes to fluxes. We found that the best fitting models are around 12 solar masses  $M_{\odot}$  (Figure 7). We then ran the SNEC code with a finer parameter space, between 11 and 12.5  $M_{\odot}$  ( $\Delta M = 0.5 M_{\odot}$ ), and again between  $0.2$  and  $1.2 \times 10^{51}$  erg

$\Delta t$ (Days)	$\nu$ (GHz)	$F_{\nu}$ (mJy)	Configuration
51	5	$0.32 \pm 0.04$	B
51	7	$0.19 \pm 0.02$	B
51	22	$0.08 \pm 0.02$	B
57	2.5	$0.26 \pm 0.05$	B
57	3.5	$0.26 \pm 0.04$	B
57	5	$0.25 \pm 0.03$	B
57	7	$0.19 \pm 0.03$	B
57	10	$0.12 \pm 0.02$	B
57	15	$0.08 \pm 0.02$	B
104	2.31	$0.59 \pm 0.09$	B => A
104	2.94	$0.39 \pm 0.06$	B => A
104	3.63	$0.33 \pm 0.05$	B => A
104	5	$0.22 \pm 0.03$	B => A
104	7	$0.14 \pm 0.03$	B => A
104	10	$0.09 \pm 0.02$	B => A
104	15	$0.06 \pm 0.01$	B => A
136	2.31	$0.33 \pm 0.05$	BnA => A
136	2.94	$0.31 \pm 0.04$	BnA => A
136	3.63	$0.24 \pm 0.05$	BnA => A
136	6	$0.13 \pm 0.02$	BnA => A
136	10	$0.07 \pm 0.01$	BnA => A
136	15	$0.04 \pm 0.01$	BnA => A

**Table 1.** A summary of the radio observations of SN 2020qmp.  $\Delta t$  is the midpoint between the optical last non-detection and the optical discovery.  $\nu$  is the observed frequency in GHz.

( $\Delta E = 0.1 \times 10^{51}$  erg), and repeat the  $\chi^2$  analysis to obtain the final best-fitting progenitor mass as well as explosion energy. The results of the analysis are shown in Figure 7, and we obtain a best-fit ZAMS progenitor mass of  $12.5 M_{\odot}$ , and an initial explosion energy of  $0.5 \times 10^{51}$  erg. The best-fit model LCs along with the observed LCs are presented in Figure 8. This best-fit mass matches well with the ZAMS progenitor mass obtained using an independent method in §4 using the nebular spectra. However, it is important to note that this is only a crude estimate of the ZAMS progenitor mass as the LC modeling was able constrain the explosion energy well, but less so for the masses (as seen in Figure 7). Therefore, it was necessary to combine results from the LC modeling and nebular spectrum analysis to better constrain the ZAMS mass.

We note that it is also possible to investigate the effects of the circumstellar medium (CSM) on the early LC, through varying the constant wind density  $K$  which extends up to a radius  $R_{\text{ext}}$  (eg. Dong et al. 2020).  $K$  is dependent on both the mass loss rate of the progenitor star, as well as its wind velocity. However, SNEC assumes a standard CSM interaction model with a density profile ( $\rho(r)$ ) that goes as

$$\rho(r) = \frac{\dot{M}}{4\pi r^2 v_{\text{wind}}} = \frac{K}{r^2}, \quad (1)$$

where  $\dot{M}$  is the mass loss rate,  $r$  is the radius, and  $v_{\text{wind}}$  is the wind velocity. However, it is not certain that this density profile holds when combining radio and X-ray observations of the SN, as the SN shows possible deviations from a standard CSM interaction model (see §5). Therefore, we do not perform further analysis varying  $K$  and  $R_{\text{ext}}$ .

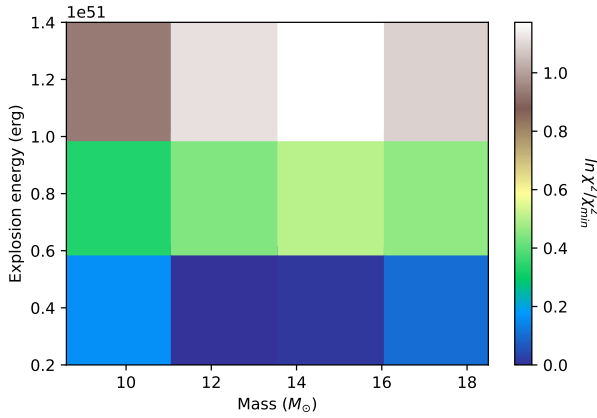


**Fig. 7.** Top panel: The  $\chi^2$  values for the different LC models compared to observations, over a range of 10 to 17.5  $M_{\odot}$  ( $\Delta M = 2.5 M_{\odot}$ ) and an explosion energy of 0.2 to  $1.2 \times 10^{51}$  erg ( $\Delta E = 0.4 \times 10^{51}$ ). Bottom panel: The  $\chi^2$  values for the different LC models compared to observations, over a range of 11.25 to 12.75  $M_{\odot}$  ( $\Delta M = 0.25 M_{\odot}$ ) and an explosion energy of 0.2 to  $1.2 \times 10^{51}$  ergs ( $\Delta E = 0.1 \times 10^{51}$ ), with an "X" demarcating the best-fit model.

#### 4. Nebular Spectrum Analysis

After the photosphere recedes into the ejecta after the hydrogen recombination plateau ends, the ejecta become optically thin in the continuum and the inner regions become visible, providing insights into the nucleosynthesis in the explosion. During this phase, the luminosity becomes directly proportional to how much  $^{56}\text{Ni}$  was created during the explosion. A spectrum taken in this phase allows us to infer the nucleosynthetic yields of the explosion, which allows for the measurement of the ZAMS progenitor mass through the comparison of line strengths with existing models, as nucleosynthesis is strongly dependent on the mass of the progenitor. This phase of the LC is called the nebular phase, where powering of the LC becomes dominated by the radioactive decay of  $^{56}\text{Co}$ . In particular, the comparison of the intensities of the [O I] doublet has been shown to provide a good indication of the zero-age main-sequence (ZAMS) mass (Uomoto 1986; Jerkstrand et al. 2014), which we use in our analysis.

Jerkstrand et al. (2014) developed the models that we use in our analysis. They started with evolved ejecta exploded using the hydrodynamic code KEPLER (Woosley & Heger 2007), and created the spectra through using a radiative transfer code CMFGEN (Jerkstrand 2011). The models are computed at dif-

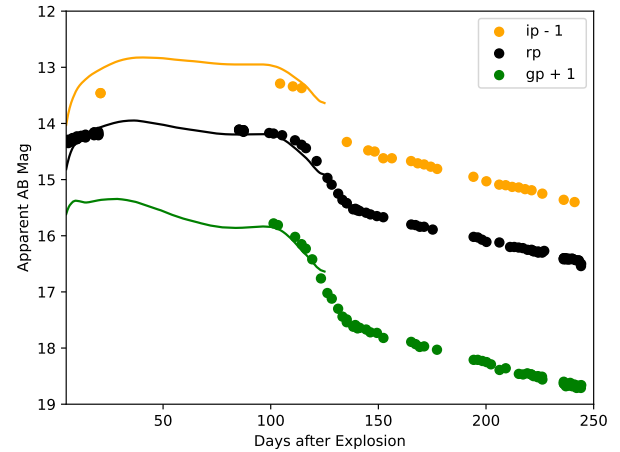


**Fig. 8.** The best-fit LC models in  $i$ ,  $r$ , and  $g$  bands, representing a progenitor star of  $12.5 M_{\odot}$  and an initial explosion energy of  $0.5 \times 10^{51}$  ergs. The models were fit to the observed LC up to 125 days after the explosion.

ferent time epochs after the explosion, for ZAMS masses of 9, 12, 15, 19, and  $25 M_{\odot}$ , provided by Jerkstrand et al. (2014) and Jerkstrand et al. (2018). Using these models, along with our observed spectra, we then estimated the ZAMS mass of the progenitor star, by first calculating the  $^{56}\text{Ni}$  mass, and then comparing the [O I] doublet line luminosity normalized relative to the  $^{56}\text{Co}$  decay power.

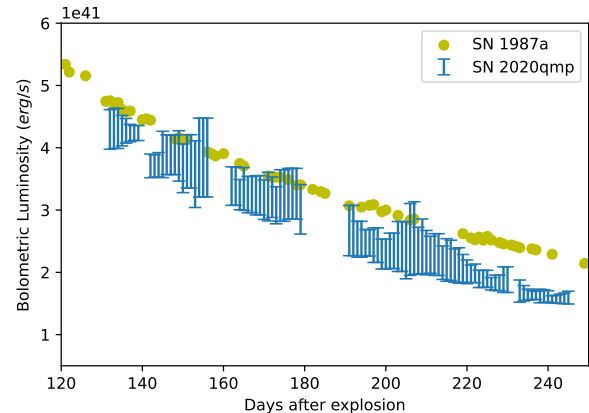


**Fig. 9.** Zoom in of the radioactive decay tail of the bolometric LCs of SN2020qmp and SN 1987A from the top panel.

##### 4.1. $^{56}\text{Ni}$ Mass Calculation

It is well known that the nebular phase of Type II SNe is powered through the nuclear radioactive decay of  $^{56}\text{Ni}$  to  $^{56}\text{Co}$ , and then to  $^{56}\text{Fe}$ . During this process,  $\gamma$ -rays and positrons are released; however, at this point the ejecta are still not transparent to  $\gamma$ -rays, and as a result the bolometric luminosity during the nebular phase can be used to determine the  $^{56}\text{Ni}$  mass through the relation (Spiro et al. 2014):

$$M_{SN}(\text{Ni}) = 0.075 \times L_{SN}/L_{87A} M_{\odot}, \quad (2)$$

where  $L_{SN}$  is the bolometric luminosity of the SN in question, and  $L_{87A}$  is the bolometric luminosity of SN 1987A.

We re-compute the bolometric LC of SN 2020qmp in this section over just the  $r$ ,  $g$ , and  $i$  filters, using the same method described in §2.1, in order to make a comparison with the bolometric LC of SN 1987A, over the B, V, R, and I filters. In Figure 9, we overlay the tail-end of the bolometric LCs of SN 2020qmp and SN 1987A<sup>5</sup>. We derived the luminosity through fitting best-fit lines for SN 2020qmp and SN 1987A in its tail-end radioactive decay phase, and comparing the y-intercepts of the two lines through Eq. 2 to obtain  $M_{SN}(\text{Ni}) = 0.06^{+0.02}_{-0.01} M_{\odot}$ .

#### 4.2. Normalized $[\text{O I}]$ Line Luminosity and ZAMS Mass

After obtaining the  $^{56}\text{Ni}$  mass, we then calculated the normalized  $[\text{O I}]$  doublet line luminosity, relative to the  $^{56}\text{Co}$  decay power, which is the main characteristic used to compare model spectra to the observed spectrum. The normalized luminosity is given by Jerkstrand et al. (2015) as,

$$L_{\text{norm}}(t) = \frac{L_{\text{line}}}{1.06 \times 10^{42} \frac{M_{\text{Ni}}}{0.075 M_{\odot}} (e^{-t/111.4d} - e^{-t/8.8d}) \text{ erg s}^{-1}}. \quad (3)$$

Using the  $^{56}\text{Ni}$  mass obtained from the photometry, as well as the line luminosity for the  $[\text{O I}]$  doublet (through integrating the line flux subtracted from the continuum by fitting a double-peaked Gaussian function to the spectra) we then obtain normalized line luminosities at 211 days and 266 days after the explosion through Eq. 3 ( $1.8 \times 10^{-14}$  and  $4.2 \times 10^{-14}$   $\text{erg s}^{-1}$ ). We also note that before calculating these luminosities, we scaled the spectra to match the photometry obtained by ZTF at the same epoch in order to get absolute flux calibration. Then, going through the same process of fitting a double-peaked Gaussian for each of our model spectra, and assuming the same  $^{56}\text{Ni}$  mass, we also obtained normalized line luminosities for each model spectra and compare the results in Figure 10. We see that the normalized luminosities obtained for the observed spectra and  $12 M_{\odot}$  model are equivalent within error bars. This allows us to infer that the progenitor star was close to  $12 M_{\odot}$ . These results agree with the results found in §3, which gave us a progenitor mass of around  $12.5 M_{\odot}$ .

#### 5. Modeling the Radio Data Combined with Optical and X-ray

The radio spectra obtained with the VLA (as described in §2.4) are presented in Figure 11. The SN exhibits an optically thin emission 51 days after the explosion (at  $\geq 5$  GHz; no lower frequencies were observed at that epoch), while the 57-day spectrum shows a turnover at around 4 GHz into an optically thick spectrum. However, the turnover frequency is not well constrained due to scarce data in the optically thick regime. On day 104, an optically thin spectrum is observed down to a frequency of 2.31 GHz, surprisingly at a significantly higher flux density at frequencies lower than the turnover frequency observed earlier. The last spectrum, 136 days after the explosion, exhibits an optically thin emission with a possible turnover at the lowest observed frequency at around 2.3 GHz. This turnover frequency is even less constrained than the one at 57 days after the explosion. In the following section, we discuss the radio data in light of an SN-CSM interaction model and derive the shock physical parameters, e.g. radius and magnetic field strength, and the inferred shock velocity and progenitor's mass-loss rate. We also discuss

<sup>5</sup> LC compiled from the Open Supernova Catalog: <https://sne.space> (Guillochon et al. 2017)

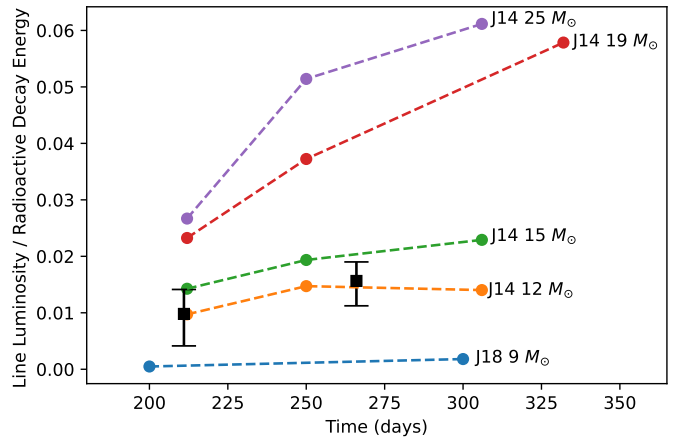


**Fig. 10.** The normalized line luminosities of the  $[\text{O I}]$  doublet ( $\lambda 6300, 6364 \text{ \AA}$ ) at different time epochs for the observed spectra of SN 2020qmp as well as the models from Jerkstrand et al. (2014) and Jerkstrand et al. (2018). The observed luminosities from SN 2020qmp are plotted as squares with their error bars in black, while each of the models are plotted with circles with different colors corresponding to the models.

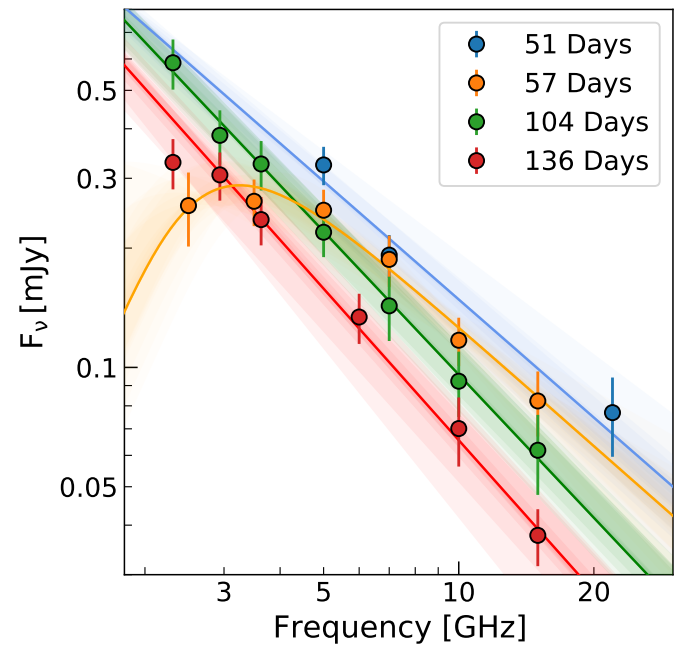


**Fig. 11.** VLA radio spectral energy distributions of SN 2020qmp at four different epochs. The lines are fitted models as discussed in §5.1, with a shaded confidence region of  $1\sigma$ . A two power law model as presented in Eq. 4 in Chevalier (1998), was fitted to the spectrum 57 days after the explosion. An optically thin power law model was fitted to the spectra 51, 104, and 136 days after the explosion.

the possibility of a variable CSM density structure suggested by the temporal evolution of the radio spectrum. Then, we use the X-ray and optical data combined with the radio to estimate the shock micro-physical parameters and discuss their effects on our estimates of the shock properties.

### 5.1. Modeling the Radio Spectra

When the SN ejecta interacts with the CSM, it drives a shock-wave into the CSM. At the shock front, electrons are accelerated to relativistic velocities with a power-law energy density distribution,  $N(E) \propto E^{-p}$ , where  $p$  is the electron spectral index. The magnetic field is also enhanced at the shock front. The relativistic electrons that gyrate in the presence of that magnetic field give rise to synchrotron emission which is usually observed at radio frequencies (Chevalier 1982). The intrinsic synchrotron emission might be absorbed by synchrotron self-absorption (SSA; Chevalier 1998) and/or free-free absorption (FFA; Weiler et al. 2002). The optically thin regime of the spectrum is expected to follow a power-law function ( $F_\nu \propto \nu^{-\beta}$ ), when in the absence of cooling (e.g. inverse Compton cooling), we expect a constant power-law  $\beta = (p - 1)/2$ . The full shape of the spectrum as a function of the radio-emitting shell radius and the magnetic field strength is shown in Eq. 1 in Chevalier (1998).

Chevalier & Fransson (2006) have shown that in the case of a synchrotron self-absorbed spectrum, the radius of the synchrotron emitting shell, and the magnetic field strength can be obtained when the radio spectral peak is observed. For a spectrum with an observed peak flux density  $F_{\nu_a}$  at a frequency  $\nu_a$ , assuming a typical power-law index  $p = 3$  (Chevalier 1998), the radius is given by

$$R = 4.0 \times 10^{14} \alpha^{-1/19} \left( \frac{f}{0.5} \right)^{-1/19} \left( \frac{F_{\nu_a}}{\text{mJy}} \right)^{9/19} \times \left( \frac{D}{\text{Mpc}} \right)^{18/19} \left( \frac{\nu_a}{5 \text{GHz}} \right)^{-1} \text{cm}, \quad (4)$$

where  $D$  is the distance to the SN,  $f$  is the emission filling factor, and the equipartition parameter  $\alpha$  is the ratio between the fraction of energy deposited by the shock to the relativistic electrons ( $\epsilon_e$ ), and the magnetic field ( $\epsilon_B$ ). The magnetic field strength, in this case, is given by

$$B = 1.1 \alpha^{-4/19} \left( \frac{f}{0.5} \right)^{-4/19} \left( \frac{F_{\nu_a}}{\text{mJy}} \right)^{-2/19} \times \left( \frac{D}{\text{Mpc}} \right)^{-4/19} \left( \frac{\nu_a}{5 \text{GHz}} \right) \text{G}. \quad (5)$$

We first modelled the optically thin spectra on 51, 104, and 136 days after the explosion as power-law functions of the form,  $F_\nu \sim \nu^{-\beta}$ . We do not use the data at the lowest frequency on day 136 as it might feature a turnover (and thus a deviation from a simple power-law function). We performed a  $\chi^2$  minimization fit. For the first spectrum (51 days), the fit resulted in  $\beta = 0.99 \pm 0.06$  with a minimum  $\chi^2 = 1.58$  and one degree of freedom (dof). However, this is based only on three data points and therefore should be treated carefully. For the spectrum on day 104, we find  $\beta = 1.20 \pm 0.06$  with a minimum  $\chi^2$  of 0.5 (and five dof). The fit of the last epoch (136 days) resulted in a power law of  $\beta = 1.27 \pm 0.06$  with a minimum  $\chi^2$  of 0.34 (and three dof). The above fits, with their  $1\sigma$  confidence interval, are shown in Figure 11. These power-laws correspond, in the non-cooling regime, to  $p = 2.98 \pm 0.12$ ,  $3.40 \pm 0.12$ , and  $3.54 \pm 0.12$ , for the first, third, and forth spectrum, respectively. However, the actual value of  $p$  will differ if cooling effects are taking place, i.e., if its real value is  $p = 3$  then the rather steep spectral slopes are due to cooling.

To derive the shock physical parameters we fit a parameterized model, similar to Eq. 4 in Chevalier (1998), to the spectrum observed at 57 days after the explosion. The free parameters are the peak flux density,  $F_{\nu_a}$ , its frequency,  $\nu_a$ , and the spectral index of the optically thin regime,  $\beta$ . We use `emcee` (Foreman-Mackey et al. 2013) to perform an MCMC analysis to determine the posteriors of the parameters of the fitted model (and use flat priors). We find, for the spectrum taken 57 days after explosion, a peak flux density of  $F_{\nu_a} = 0.28 \pm 0.03$  mJy at  $\nu_a = 2.89^{+0.53}_{-0.73}$  GHz, and an optically thick power-law of  $\beta = 1.02 \pm 0.21$ . Given these fitted parameters and assuming  $p = 3$ ,  $f = 0.5$ , and equipartition ( $\alpha = \epsilon_e/\epsilon_B = 1$ ), the radius of the emitting shell is  $R = (5.1^{+1.0}_{-1.3}) \times 10^{15}$  cm, and the magnetic field strength is  $B = 0.4 \pm 0.1$  G. Assuming a constant shock velocity, i.e.,  $v_{sh} = R/t$ , where  $t$  is the time since explosion, we derive  $v_{sh} = 1.0^{+0.2}_{-0.3} \times 10^4$  km s $^{-1}$  on day 57 after the explosion.

We next assume that the CSM, shocked by the SN ejecta, was deposited via mass-loss from the progenitor star before the explosion. Thus, the radio emission modeling can be used to estimate a mass-loss rate, assuming a constant mass-loss rate via a constant velocity stellar winds. Under this assumption, the CSM density structure has a form of  $\rho \sim \frac{\dot{M}}{v_w} r^{-2}$ , where  $\dot{M}$  is the mass-loss rate and  $v_w$  is the wind velocity. Assuming that the magnetic field energy density is a fraction  $\epsilon_B$  of the post-shock energy density  $\sim \rho v_{sh}^2$ , and a constant shock velocity, the mass-loss rate is given by

$$\dot{M} = 5.2 \times 10^{-8} \left( \frac{\epsilon_B}{0.1} \right)^{-1} \left( \frac{B}{1 \text{G}} \right)^2 \left( \frac{t}{10 \text{Days}} \right)^2 \times \left( \frac{v_w}{10 \text{km/s}} \right) \text{M}_\odot \text{yr}^{-1}. \quad (6)$$

Thus, assuming  $\epsilon_B = 0.1$ , the mass-loss rate derived from the fitted model at 57 days after explosion is  $\dot{M} = (2.9^{+1.1}_{-1.5}) \times 10^{-7} \text{ M}_\odot \text{yr}^{-1}$ , for an assumed wind velocity of 10 km/s.

### 5.2. A variable CSM density structure

The CSM interaction model with the assumptions presented above predicts a constant peak flux density density that shifts to lower frequencies with time, for an assumed CSM structure of  $r^{-2}$ . However, the peak flux density 104 days after the explosion, despite not being observed, is higher than the observed peak flux density on 57 days after the explosion. A useful tool to examine this atypical increase in the peak flux density between the two epochs is the phase space of peak radio spectral luminosity,  $L_{\nu_a}$  vs. the time of the peak,  $t_a$ , multiplied by its frequency  $\nu_a$ . Lines of equal shock velocity and equal mass-loss rate can be plotted in this phase space, also known as Chevalier's diagram (Chevalier 1998). Figure 12 is showing Chevalier's diagram for SN 2020qmp, with the radio emission spectral peak at 57 days after explosion (see §5.1). Also shown in this figure is a shaded region that marks the ruled out region due to the limit on the peak flux density and frequency 104 days after the explosion. Lines of equal shock velocities and mass-loss rates for typical values for the values derived by the peak at 57 days are also plotted. We assumed here wind velocity of 10 km s $^{-1}$  and  $p = 3$ .

Under the assumption of a constant shock velocity in the CSM and a CSM density structure of  $r^{-2}$ , the position of the peak in this phase space should remain constant over time. However, as seen in Fig. 12, the peak flux density changes significantly between the two epochs. This suggests that (when assuming a

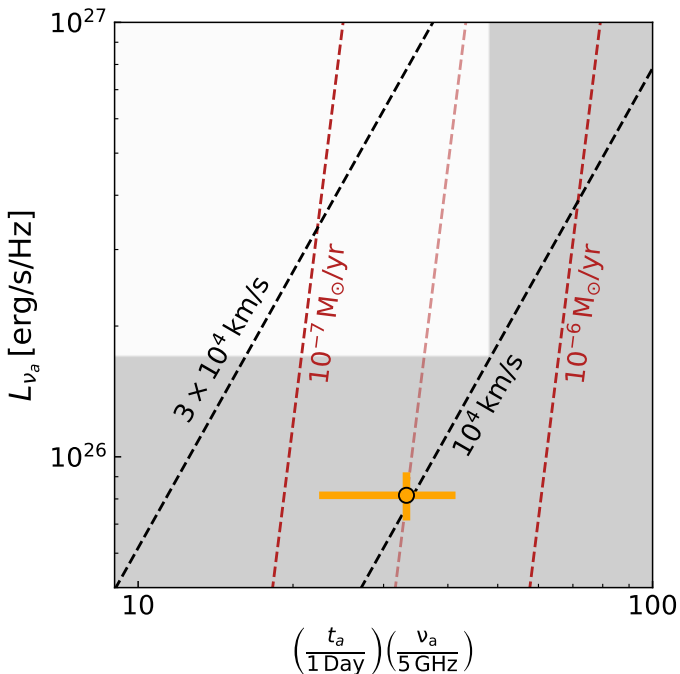


**Fig. 12.** Chevalier’s diagram for SN2020 qmp. The orange point is the position of the radio spectral peak derived 57 days after the explosion. Under the assumption of a shockwave traveling with a constant velocity in a simple  $r^{-2}$  CSM density structure, the position of the peak should remain constant. However, the shaded region, which is the ruled out region derived from the limit on the radio spectral peak on the subsequent observation (on day 104), is in disagreement with the radio spectral peak obtained before. This disagreement points towards a non-typical CSM structure. Also plotted for reference are equal lines of shock velocities and mass-loss rates (assuming wind velocity of 10 km s $^{-1}$ ).

constant shock velocity) we observe significant variations in the mass-loss rate by a factor of  $\sim 2$ . Furthermore, the lowest observed frequency on day 136 might feature a spectral turnover. If indeed that is the case, this points towards additional variability in the CSM density structure. However, we emphasize that since the possible turnover in the spectrum on day 136 is based only on one point it should be treated with caution.

### 5.3. Deviation from Equipartition

The results of our radio emission modeling above are sensitive to the assumption of the ratio between the fraction of shock energy that goes into electron acceleration ( $\epsilon_e$ ), and the fraction of energy that goes into the enhanced magnetic field ( $\epsilon_B$ ). In our analysis above we have used the common assumption of equipartition ( $\alpha \equiv \epsilon_e/\epsilon_B = 1$ ). However, deviations from equipartition have been observed before in several SNe (e.g. SN 2011dh (Soderberg et al. 2012; Horesh et al. 2013b), SN 2012aw; (Yadav et al. 2014), SN 2013df (Kamble et al. 2016), SN 2020oi; (Horesh et al. 2020)). Typically, when one has only radio data, it is difficult to determine whether this assumption holds. However, given an X-ray detection (albeit marginal), we can try to estimate these micro-physical parameters. We extrapolate the radio spectrum we observed at 57 days after explosion to the time of X-ray detection (8.8 days) according to a typical power law for the optically thin regime of  $F_\nu(t) \sim t^{-1}$  (Chevalier 1998). We then extrapolated this emission to the X-ray band according to the spectral index obtained previously for that epoch. This gives an estimated luminosity of  $2 \times 10^{36}$  erg s $^{-1}$  at the *Swift*/XRT band

on day 8.8 after the explosion. This is three orders of magnitude lower than the observed X-ray luminosity at that time. Thus, even if the extrapolation of the radio emission to early times and to the X-ray band is somewhat crude, there is evidence for excess in X-ray emission.

Björnsson & Fransson (2004) suggested inverse Compton (IC) scattering of photospheric photons by relativistic electrons at the shock front as a possible emission mechanism in the X-ray. IC scattering is also assumed to be responsible for the observed X-ray emission in several past SNe (e.g. SN 2011dh Soderberg et al. 2012; Horesh et al. 2013b, SN 2012aw; Yadav et al. 2014, SN 2013df Kamble et al. 2016, SN 2020oi; Horesh et al. 2020). Eq. 32 in Chevalier & Fransson (2006) gives the X-ray luminosity, in the case of IC scattering, as a function of the bolometric luminosity, time after the explosion, mass-loss rate, shock velocity, and the microphysical parameters. We make use of this equation to estimate the mass-loss rate given the X-ray luminosity of  $2 \times 10^{39}$  erg s $^{-1}$ , 8.8 days after the explosion, the bolometric luminosity of  $2.4 \times 10^{42}$  erg s $^{-1}$  at that time, and the assumption of equipartition. We assume a shock velocity of  $10^4$  km s $^{-1}$  based on the optical photospheric expansion velocity of  $\sim 9000$  km s $^{-1}$  from optical spectra near that time. The value of the optically derived velocity is expected to be somewhat slower than the velocity of the shock in the CSM since the optical emission originates from a deeper and slower region of the SN ejecta. We infer a mass-loss rate of  $8.3 \times 10^{-6} M_\odot/\text{yr}$  for an assumed wind velocity of 10 km s $^{-1}$ . On the other hand, the mass-loss rate derived from the radio spectrum 57 days after the explosion is smaller by a factor of  $\sim 30$  (see §5.1).

As seen above, under the assumption of equipartition, the mass-loss rate derived from the radio synchrotron emission on day 57 is in disagreement with the mass-loss rate derived from the X-ray IC emission on day 8.8. A possible explanation for this large discrepancy in the mass-loss rate estimates is deviation from equipartition, such that satisfies  $\epsilon_B = 3.1 \times 10^{-4}$ , which in turn translates to  $\alpha = 327$  (assuming a typical  $\epsilon_e = 0.1$ ). This, in turn, results in a reduction of the shockwave radius estimate (and of the shock velocity estimate) derived from the radio spectrum on day 57 by 26%. The shock velocity estimate decreases to  $v_{sh} = 7400$  km s $^{-1}$ , in this case. Alternatively, the above discrepancy can be reconciled if the progenitor star experiences huge variability (by a factor of  $\sim 30$  at least) in its mass-loss rate in the years before the explosion. While the radio data alone suggest some variability in the mass-loss rate, this variability is only by a factor of  $\sim 2$ . The level of this latter observed mass-loss rate variability is far away from the variability needed to explain the observed X-ray emission under the equipartition assumption. We emphasize that since the X-ray detection on day 8.8 is only at the level of  $2\sigma$ , any physical parameter inferred from it (i.e. mass-loss rate, shock velocity, and the microphysical parameters) should be taken with a grain of salt.

## 6. The Local CCSN rate and Near-Infrared Surveys

Most massive star formation—and consequently most CCSNe—occur in highly dust-obscured regions in the Universe. Therefore, determining the rate of CCSNe is highly dependent on the effects of dust and extinction (e.g., Grossan et al. 1999; Maiolino et al. 2002). As a NIR survey, PGIR is sensitive to CCSNe that may be obscured at optical wavelengths due to high extinction values. Though SN 2020qmp itself does not appear to be highly extinguished at optical wavelengths its discovery invites the question as to how effective NIR surveys are in detecting obscured SNe in comparison to optical surveys.

Mattila et al. (2012) derived a CCSN rate of  $7.4^{+3.7}_{-2.6} \times 10^{-4} \text{ yr}^{-1} \text{ Mpc}^{-3}$  within the local 6 Mpc volume and  $1.5^{+0.4}_{-0.3} \times 10^{-4} \text{ yr}^{-1} \text{ Mpc}^{-3}$  within the local 6–15 Mpc volume, using a 12 year sample of CCSNe from 2000–2012. However, they also derived an estimate of  $18.9^{+19.2}_{-9.5}\%$  of CCSNe missed locally by optical surveys. More recently, Jencson et al. (2019) found that this number could be as high as  $38.5^{+26.0}_{-21.9}\%$ , based on highly reddened CCSNe detected in a sample of nearby galaxies ( $D \lesssim 40$  Mpc) in the mid-infrared by the Spitzer Infrared Intensive Transient Survey (SPIRITS; Kasliwal et al. 2017). As some objects in the sample were not definitely classified as CCSNe, we consider this as a maximal estimate of the optically missed fraction. Here, we examine the sensitivity of wide-field, ground-based surveys in the NIR such as PGIR, and future surveys such as the Wide-Field Infrared Transient Explorer (WINTER), an upcoming (first light planned for Fall 2021)  $J$ -band search with a 1-m telescope at Palomar Observatory that is expected to achieve a median depth of 20.8 AB mag (Simcoe et al. 2019; Lourie et al. 2020; Frostig et al. 2020) over the entire accessible Northern sky at a cadence of a few weeks, to detect such highly obscured CCSNe in the local Universe.

Richardson et al. (2014) calculated the bias-corrected absolute magnitude distributions of SNe primarily from the Asiago Supernova Catalog (Tomasella et al. 2014) as well as a few supplemental data sources. By averaging their distributions for all types of CCSNe, and weighting them accordingly by the frequency of each subtype, we obtain an estimate of the average magnitude for any CCSN to be  $M_{\text{abs}} = -17.42 \pm 0.37$ , across all bands. Assuming this absolute magnitude for discovery, in the upper panel of Figure 13, we show the sensitivity of PGIR in the  $J$ -band to detecting CCSNe at a given distance and value of the total  $V$ -band extinction,  $A_V$ , assuming a survey depth of  $J = 15.7$  mag. To convert from  $A_V$  to  $A_J$ , the extinction value in  $J$ -band, we assume a standard extinction law with  $R_V = 3.1$  according to Fitzpatrick (1999) and use a 10000 K black-body source spectrum as an approximation to a CCSN near peak light. We also show the corresponding sensitivity curves for ZTF in the  $g$ - and  $r$ -bands, assuming a survey depth of 20.5 mag for both bands. Figure 13 shows that PGIR is more effective in detecting very highly obscured CCSNe ( $A_V \gtrsim 10$ –15 mag) in the very local universe, despite the fact that its median depth is  $\sim 5$  mag shallower than ZTF. Specifically, using the formulation detailed above, PGIR is more sensitive to these extinguished CCSNe than ZTF out to  $\sim 6.4$  Mpc in the  $r$ -band and  $\sim 12.7$  Mpc in the  $g$ -band. We also show the vast improvement in sensitivity to obscured CCSNe for WINTER, assuming a median survey depth of  $J = 20.8$  mag. We note that we do not take into account the cadence of WINTER, assuming it is sufficient to catch any SN in its active footprint near peak light.

In the bottom panel of Figure 13, we show the results of a simulation representing a distribution of CCSNe in the local 40 Mpc volume with varying levels of extinction. In order to model the extinction distribution, we pull from Jencson et al. (2019), using their sample of optically discovered CCSNe (8) and infrared-discovered confirmed (2) and candidate CCSNe (3) in the SPIRITS sample between 2014–2018. We construct an empirical extinction distribution based on the reported values of  $A_V$  for each object. Three of the infrared-discovered objects were undetected in the optical, and thus only lower limits on  $A_V$  for these sources were available. We assign them values  $A_V = 8$  mag in the distribution, the highest measured value of any object in the sample, and emphasize again that we consider this as a *maximal* estimate of the fraction of highly reddened CCSNe.

We then fit a power law to the cumulative distribution of measured  $A_V$  values, and from there derive a probability distribution function for the extinction values of CCSNe. Next, we derive a probability distribution for the distances of CCSNe that are uniformly distributed throughout the local 40 Mpc volume, where we adopt the volumetric CCSN rate of Mattila et al. (2012) mentioned above for  $D < 6$  Mpc and apply the 6–15 Mpc value for larger distances. For an assumed active areal survey coverage of 15,000 sq. deg (approximately the entire accessible northern sky from Palomar at any given time), we thus expect 75 total CCSNe within the 40 Mpc volume in a 5-year period that fall within the active survey footprint of PGIR, ZTF or WINTER.

Finally, we run the simulation by distributing these 75 hypothetical CCSNe randomly in distance and  $A_V$  according to the probability distributions derived above, and repeat the simulation 10 times. A single instance of our simulation is shown in Figure 13. We caution that the spread of CCSNe at high extinction values above  $A_V \gtrsim 8$  mag is based on an extrapolation of the empirical distribution derived from the SPIRITS sample, and should be taken with a grain of salt. Events that fall below a given sensitivity curve are counted as “detected” by the respective survey. On average over the 10 simulations, we find that PGIR is expected to detect only around 0.1 CCSNe that ZTF would miss due to dust extinction in a five year time period. This is mainly attributable to the fact that PGIR’s median depth (15.7 AB mag) is much lower than that of ZTF (20.5 AB mag). However, when looking at future NIR surveys such as WINTER, we find a much higher number of projected CCSNe that would be missed by ZTF but are accessible to WINTER, namely 13.6 CCSNe ( $\approx 18\%$  of the 75 total) averaged over our 10 simulations. WINTER’s median depth (20.8 AB mag) is around the same as ZTF’s, and clearly demonstrates the advantage that employing NIR surveys can have on discovering highly reddened CCSNe in the future. While this simulation is based on the assumption of maximal estimate of the number of highly reddened SNe, it demonstrates that a 5-year SN search with a deep, wide-field survey with WINTER will have sufficient number statistics to accurately constrain the high end of the extinction distribution for CCSNe in the local Universe.

## 7. Conclusions

In this paper, we presented a detailed, multi-wavelength analysis of SN 2020qmp discovered by PGIR. Based on characteristic hydrogen lines in its spectra, along with a long plateau in its optical LC, the SN can be classified as a Type IIP SN. We do not detect any polarization from the SN during the plateau phase, which is expected because the outer ejecta visible during this phase are generally symmetric (Wang & Wheeler 2008). Through hydrodynamical LC modeling using SNEC, we obtain a best-fit progenitor mass of around  $12.5 M_{\odot}$  and explosion energy of  $0.5 \times 10^{51}$  erg, which are values comparable to those obtained in analyses done of other Type IIP progenitors (Anderson et al. 2014; Sanders et al. 2015). By comparing the normalized line luminosities of the [O I] doublet (relative to the  $^{56}\text{Co}$  decay energy) between the observed spectrum and Jerkstrand et al. (2014) models, we estimate the progenitor mass of the SN to be  $\approx 12 M_{\odot}$ , consistent with the results found through the hydrodynamical LC modeling.

We also made use of broadband radio observations conducted with the VLA to derive the physical properties of the shock in the CSM under the CSM interaction model. Assuming equipartition between the fraction of energy in the electron ( $\epsilon_e$ ), and the fraction of energy in the enhanced magnetic

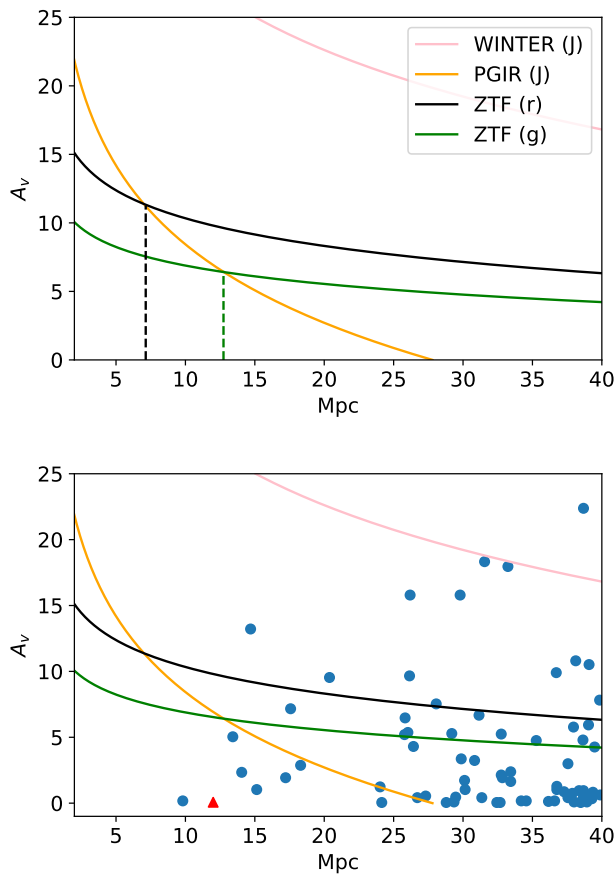


**Fig. 13.** *Top panel:* Comparison of PGIR’s sensitivity to detecting CCSNe as a function of distance and extinction to that of ZTF’s  $r$  and  $g$  bands, assuming an absolute AB magnitude of -17.42 for every SNe. The proposed WINTER survey’s sensitivity is also shown. The vertical lines are the distances (in Mpc) where PGIR is more sensitive to extinguished CCSNe than ZTF. *Bottom panel:* Simulated SNe over a five year span using an extinction distribution derived from the CCSN candidate sample of Jencson et al. (2019). Details of the simulation are given in the main text, and the sensitivity curves are the same as in the top panel. SN 2020qmp in particular is marked in red and as a triangle to demonstrate its placing compared to the simulated distribution.

field ( $\epsilon_B$ ), the radio spectrum 57 days after the explosion gives a shock velocity  $v_{sh} = 10^4 \text{ km s}^{-1}$ , and a mass loss rate of  $\dot{M} = (2.9_{-1.5}^{+1.1}) \times 10^{-7} \text{ M}_\odot \text{ yr}^{-1}$ , for an assumed wind velocity of  $10 \text{ km s}^{-1}$ , which is within the range of most RSG progenitors for Type IIP SN (Smith 2014). However, the radio spectrum on day 104 showed a surprisingly higher peak flux density at lower frequency than the one observed on day 57. We determine that assuming standard CSM interaction models, and constant shock velocity, an increase in mass-loss rate by a factor of  $\sim 2$  is needed to explain this discrepancy. This and additional radio observations on day 136 points to variability in the progenitor mass-loss rate during the 1000 years prior to explosion.

Early X-ray observations with Swift/XRT show tentative excess emission compared to observations extrapolated to the same epoch from radio frequencies using a standard shockwave evolution. Assuming that this emission excess originates from inverse Compton scattering of photospheric photons by relativistic electrons in the shock front, we derive a much greater mass-loss rate than the one derived by the radio spectrum on day 57, of  $\dot{M} = 8.3 \times 10^{-6} \text{ M}_\odot \text{ yr}^{-1}$ , for an assumed wind velocity of

$10 \text{ km s}^{-1}$ . This discrepancy can be resolved assuming deviation from equipartition and  $\epsilon_B = 0.00031$  and  $\epsilon_e = 0.1$ . This also calls for a reduction in the inferred shock velocity by 26%, from  $10^4 \text{ km s}^{-1}$  to  $7400 \text{ km s}^{-1}$ . One can also explain the difference in mass-loss rates by extreme mass-loss variations from the progenitor in the years prior to the explosion.

Finally, we created a simulation of CCSNe within a five year span, assuming CCSN rates from Mattila et al. (2012), and extrapolating an extinction distribution from Jencson et al. (2019), assuming an absolute magnitude of  $-17.42 \pm 0.37$  for every SN calculated through taking a weighted distribution of the CCSNe sample given in Richardson et al. (2014). Though SN 2020qmp itself is not extremely extinguished with  $A_v = 0.0669$  (Schlafly & Finkbeiner 2011), its discovery prompted the question as to how much more sensitive PGIR is than optical surveys such as ZTF to extinguished SNe as a NIR survey. We find that in a five year span, we expect PGIR to detect around 0.1 CCSNe that ZTF misses, and this low number is due to the extremely lower median depth that PGIR has (15.7 AB mag), in comparison to ZTF (20.8 AB mag). However, this number shoots up when looking at future NIR surveys such as WINTER, with higher median depths (21 AB mag in  $J$  band), where we estimate around 13.6 CCSNe to be discovered that are missed by ZTF. This shows how promising future NIR surveys will be for discovering extinguished CCSNe.

## 8. Acknowledgements

Palomar Gattini-IR (PGIR) is generously funded by Caltech, Australian National University, the Mt Cuba Foundation, the Heising Simons Foundation, the Binational Science Foundation. PGIR is a collaborative project among Caltech, Australian National University, University of New South Wales, Columbia University and the Weizmann Institute of Science. MMK acknowledges generous support from the David and Lucille Packard Foundation. MMK and EO acknowledge the US-Israel Bi-national Science Foundation Grant 2016227. MMK and JLS acknowledge the Heising-Simons foundation for support via a Scialog fellowship of the Research Corporation. MMK and AMM acknowledge the Mt Cuba foundation. J. Soon is supported by an Australian Government Research Training Program (RTP) Scholarship. A.H. acknowledges support by the I-Core Program of the Planning and Budgeting Committee and the Israel Science Foundation, and support by ISF grant 647/18. This research was supported by Grant No. 2018154 from the United States-Israel Binational Science Foundation (BSF). We thank the National Radio Astronomy Observatory (NRAO) for conducting the radio observations with the Karl G. Jansky Very Large Array (VLA). Some of the data presented here were obtained with the Visiting Astronomer facility at the Infrared Telescope Facility, which is operated by the University of Hawaii under contract 80HQTR19D0030 with the National Aeronautics and Space Administration. Some of the data presented herein were obtained at the W.M. Keck Observatory, which is operated as a scientific partnership among the California Institute of Technology, the University of California and the National Aeronautics and Space Administration. The Observatory was made possible by the generous financial support of the W.M. Keck Foundation. SED Machine is based upon work supported by the National Science Foundation under Grant No. 1106171. The authors wish to recognize and acknowledge the very significant cultural role and reverence that the summit of Mauna Kea has always had within the indigenous Hawaiian community. We are most fortunate to have the opportunity to conduct observations

from this mountain. Based on observations obtained with the Samuel Oschin Telescope 48-inch and the 60-inch Telescope at the Palomar Observatory as part of the Zwicky Transient Facility project. ZTF is supported by the National Science Foundation under Grant No. AST-1440341 and a collaboration including Caltech, IPAC, the Weizmann Institute for Science, the Oskar Klein Center at Stockholm University, the University of Maryland, the University of Washington, Deutsches Elektronen-Synchrotron and Humboldt University, Los Alamos National Laboratories, the TANGO Consortium of Taiwan, the University of Wisconsin at Milwaukee, and Lawrence Berkeley National Laboratories. Operations are conducted by COO, IPAC, and UW. We thank Yize Dong for his help with the hydrodynamical LC modeling. We thank David Kaplan for his helpful comments before submission to the journal.

## References

Anderson, J. P., González-Gaitán, S., Hamuy, M., et al. 2014, The Astrophysical Journal, 786, 67

Bellm, E. C., Kulkarni, S. R., Graham, M. J., et al. 2019, PASP, 131, 018002

Ben-Ami, S., Gal-Yam, A., Filippenko, A. V., et al. 2012, ApJ, 760, L33

Berger, E., Kulkarni, S. R., & Chevalier, R. A. 2002, ApJ, 577, L5

Björnsson, C.-I. & Fransson, C. 2004, ApJ, 605, 823

Blagorodnova, N., Neill, J. D., Walters, R., et al. 2018, Publications of the Astronomical Society of the Pacific, 130, 035003

Branch, D. & Wheeler, J. C. 2017, Type IIP Supernovae (Berlin, Heidelberg: Springer Berlin Heidelberg), 245–265

Breeveld, A. A., Landsman, W., Holland, S. T., et al. 2011, in American Institute of Physics Conference Series, Vol. 1358, American Institute of Physics Conference Series, ed. J. E. McEnery, J. L. Racusin, & N. Gehrels, 373–376

Burrows, D. N., Hill, J. E., Nousek, J. A., et al. 2005, Space Sci. Rev., 120, 165

Chevalier, R. A. 1982, ApJ, 259, 302

Chevalier, R. A. 1998, ApJ, 499, 810

Chevalier, R. A. & Fransson, C. 2006, ApJ, 651, 381

De, K., Hankins, M., Kasliwal, M. M., et al. 2020a, PASP, 132, 025001

De, K., Hankins, M., Kasliwal, M. M., et al. 2020b, The Astronomer's Telegram, 13909, 1

De, K., Kasliwal, M. M., Hankins, M. J., et al. 2021, ApJ, 912, 19

Dekany, R., Smith, R. M., Riddle, R., et al. 2020, PASP, 132, 038001

Dessart, L., Livne, E., & Waldman, R. 2010, MNRAS, 408, 827

Dong, Y., Valenti, S., Bostroem, K. A., et al. 2020, ApJ, 906, 56

Evans, P. A., Beardmore, A. P., Page, K. L., et al. 2009, MNRAS, 397, 1177

Evans, P. A., Beardmore, A. P., Page, K. L., et al. 2007, A&A, 469, 379

Filippenko, A. V. 1997, Annual Review of Astronomy and Astrophysics, 35, 309

Fitzpatrick, E. L. 1999, PASP, 111, 63

Foreman-Mackey, D., Hogg, D. W., Lang, D., & Goodman, J. 2013, Publications of the Astronomical Society of the Pacific, 125, 306

Frostig, D., Baker, J. W., Brown, J., et al. 2020, in Society of Photo-Optical Instrumentation Engineers (SPIE) Conference Series, Vol. 11447, Society of Photo-Optical Instrumentation Engineers (SPIE) Conference Series, 1144767

Gal-Yam, A. 2017, Observational and Physical Classification of Supernovae, ed. A. W. Alsabti & P. Murdin (Cham: Springer International Publishing), 195–237

Gehrels, N., Chincarini, G., Giommi, P., et al. 2004, The Astrophysical Journal, 611, 1005

Goldberg, J. A., Bildsten, L., & Paxton, B. 2019, ApJ, 879, 3

Graham, M. J., Kulkarni, S. R., Bellm, E. C., et al. 2019, PASP, 131, 078001

Grossan, B., Spillar, E., Tripp, R., et al. 1999, AJ, 118, 705

Guillochon, J., Parrent, J., Kelley, L. Z., & Margutti, R. 2017, ApJ, 835, 64

Herter, T. L., Henderson, C. P., Wilson, J. C., et al. 2008, in Society of Photo-Optical Instrumentation Engineers (SPIE) Conference Series, Vol. 7014, Ground-based and Airborne Instrumentation for Astronomy II, ed. I. S. McLean & M. M. Casali, 70140X

Hi4PI Collaboration, Ben Bekhti, N., Flöer, L., et al. 2016, A&A, 594, A116

Horesh, A., Sfaradi, I., Ergon, M., et al. 2020, ApJ, 903, 132

Horesh, A., Stockdale, C., Fox, D. B., et al. 2013a, MNRAS, 436, 1258

Horesh, A., Stockdale, C., Fox, D. B., et al. 2013b, MNRAS, 436, 1258

Jencson, J. E., Kasliwal, M. M., Adams, S. M., et al. 2019, ApJ, 886, 40

Jerkstrand, A. 2011, PhD thesis, -

Jerkstrand, A., Ergon, M., Smartt, S. J., et al. 2015, A&A, 573, A12

Jerkstrand, A., Ertl, T., Janka, H. T., et al. 2018, MNRAS, 475, 277

Jerkstrand, A., Fransson, C., Maguire, K., et al. 2012, A&A, 546, A28

Jerkstrand, A., Smartt, S. J., Fraser, M., et al. 2014, MNRAS, 439, 3694

Kaiser, N., Aussel, H., Burke, B. E., et al. 2002, in Society of Photo-Optical Instrumentation Engineers (SPIE) Conference Series, Vol. 4836, Survey and Other Telescope Technologies and Discoveries, ed. J. A. Tyson & S. Wolff, 154–164

Kamble, A., Margutti, R., Soderberg, A. M., et al. 2016, The Astrophysical Journal, 818, 111

Kasliwal, M. M., Bally, J., Masci, F., et al. 2017, ApJ, 839, 88

Leonard, D. C., Filippenko, A. V., Ganeshalingam, M., et al. 2006, Nature, 440, 505

Lourie, N. P., Baker, J. W., Burruss, R. S., et al. 2020, in Society of Photo-Optical Instrumentation Engineers (SPIE) Conference Series, Vol. 11447, Society of Photo-Optical Instrumentation Engineers (SPIE) Conference Series, 114479K

Maiolino, R., Vanzi, L., Mannucci, F., et al. 2002, A&A, 389, 84

Martin, E. C., Fitzgerald, M. P., McLean, I. S., et al. 2018, in Society of Photo-Optical Instrumentation Engineers (SPIE) Conference Series, Vol. 10702, Ground-based and Airborne Instrumentation for Astronomy VII, ed. C. J. Evans, L. Simard, & H. Takami, 107020A

Martinez, L. & Bersten, M. C. 2019, A&A, 629, A124

Masci, F. J., Laher, R. R., Rusholme, B., et al. 2019, PASP, 131, 018003

Mattila, S., Dahlen, T., Efstathiou, A., et al. 2012, ApJ, 756, 111

McMullin, J. P., Waters, B., Schiebel, D., Young, W., & Golap, K. 2007, in Astronomical Society of the Pacific Conference Series, Vol. 376, Astronomical Data Analysis Software and Systems XVI, ed. R. A. Shaw, F. Hill, & D. J. Bell, 127

Moore, A. & Kasliwal, M. 2019, Nature Astronomy, 3, 109

Morozova, V., Piro, A. L., Renzo, M., et al. 2015, ApJ, 814, 63

Morozova, V., Piro, A. L., & Valenti, S. 2017, ApJ, 838, 28

Morozova, V., Piro, A. L., & Valenti, S. 2018, ApJ, 858, 15

Nagao, T., Maeda, K., & Tanaka, M. 2017, ApJ, 847, 111

Nagao, T., Maeda, K., & Tanaka, M. 2018, ApJ, 861, 1

Nakamura, K., Horiuchi, S., Tanaka, M., et al. 2016, MNRAS, 461, 3296

Oke, J. B., Cohen, J. G., Carr, M., et al. 1995, PASP, 107, 375

Oke, J. B. & Gunn, J. E. 1982, Publications of the Astronomical Society of the Pacific, 94, 586

Rabinak, I. & Waxman, E. 2011, The Astrophysical Journal, 728, 63

Rayner, J. T., Toomey, D. W., Onaka, P. M., et al. 2003, Publications of the Astronomical Society of the Pacific, 115, 362

Richardson, D., Jenkins, Robert L., I., Wright, J., & Maddox, L. 2014, AJ, 147, 118

Rigault, M., Neill, J. D., Blagorodnova, N., et al. 2019, A&A, 627, A115

Roming, P. W. A., Kennedy, T. E., Mason, K. O., et al. 2005, Space Sci. Rev., 120, 95

Sanders, N. E., Soderberg, A. M., Gezari, S., et al. 2015, The Astrophysical Journal, 799, 208

Sapir, N. & Waxman, E. 2017, The Astrophysical Journal, 838, 130

Schlafly, E. F. & Finkbeiner, D. P. 2011, ApJ, 737, 103

Shivvers, I., Groh, J. H., Mauerhan, J. C., et al. 2015, The Astrophysical Journal, 806, 213

Simcoe, R. A., Fűrész, G., Sullivan, P. W., et al. 2019, AJ, 157, 46

Sivanandam, S., Chapman, S., Simard, L., et al. 2018, in Ground-based and Airborne Instrumentation for Astronomy VII, ed. C. J. Evans, L. Simard, & H. Takami, Vol. 10702, International Society for Optics and Photonics (SPIE), 456–467

Smartt, S. J. 2009, ARA&A, 47, 63

Smartt, S. J. 2015, PASA, 32, e016

Smith, N. 2014, Annual Review of Astronomy and Astrophysics, 52, 487–528

Soderberg, A. M., Margutti, R., Zauderer, B. A., et al. 2012, ApJ, 752, 78

Sukhbold, T., Ertl, T., Woosley, S. E., Brown, J. M., & Janka, H. T. 2016, ApJ, 821, 38

Tinyanont, S., Millar-Blanchaer, M. A., Nilsson, R., et al. 2019, PASP, 131, 025001

Tomasella, L., Benetti, S., Cappellaro, E., et al. 2014, Astronomische Nachrichten, 335, 841

Tully, R. B., Courtois, H. M., & Sorce, J. G. 2016, AJ, 152, 50

Uomoto, A. 1986, ApJ, 310, L35

Utrobin, V. P. & Chugai, N. N. 2009, A&A, 506, 829

Utrobin, V. P. & Chugai, N. N. 2015, A&A, 575, A100

Utrobin, V. P. & Chugai, N. N. 2017, MNRAS, 472, 5004

Wang, L. & Wheeler, J. C. 2008, ARA&A, 46, 433

Weiler, K. W., Panagia, N., Montes, M. J., & Sramek, R. A. 2002, Annual Review of Astronomy and Astrophysics, 40, 387

Woosley, S. E. & Heger, A. 2007, Phys. Rep., 442, 269

Yadav, N., Ray, A., Chakraborti, S., et al. 2014, ApJ, 782, 30